PHYSICAL REVIEW B **95**, 035206 (2017)

Homogeneous versus composite $Cd_{1-x-y}Mn_xZn_ySnAs_2$ crystals: Magnetic interactions and transport properties

L. Kilanski,[*] P. Skupiński, S. Lewińska, E. Dynowska, A. Reszka, K. Grasza, R. Szymczak, A. Ślawska-Waniewska,
M. Górska, B. J. Kowalski, and W. Dobrowolski
Institute of Physics, Polish Academy of Sciences, Aleja Lotnikow 32/46, PL-02668 Warsaw, Poland

(Received 31 October 2016; published 18 January 2017)

We present the studies of structural, magnetic, and magnetotransport properties of $Cd_{1-x-y}Mn_xZn_ySnAs_2$ crystals with the average Mn contents x changing from 0.013 to 0.170 and Zn contents y varying from 0.002 to 0.051. Homogenous distribution of Mn ions is observed for the samples with $x \leqslant 0.025$. The presence of MnAs clusters in the studied alloy for $x > 0.025$ induces room-temperature ferromagnetism with the Curie temperature T_C, with values around 325 K. High crystal quality leads to high carrier mobility values observed for all of our samples, as high as 7100 $cm^2/(V\,s)$ for $x = 0.025$ and $y = 0.028$. The Shubnikov–de Haas oscillations are observed at $T \leqslant 50$ K for all of our samples. The oscillations allowed the calculation of the effective mass m^*, giving values of about $0.11–0.12 m_e$. The presence of magnetic impurities has a strong influence on the magnetoresistance of the alloy. For the samples with $x \geqslant 0.076$, the Shubnikov–de Haas oscillations are observed on the background of a strong linear positive magnetoresistance, present up to room temperature. The maximum values of the linear positive magnetoresistance are close to 200% for the sample with $x = 0.170$ and $y = 0.002$, at $T = 1.5$ K. This positive magnetoresistance is related to the presence of MnAs clusters in the semiconductor lattice.

DOI: 10.1103/PhysRevB.95.035206

I. INTRODUCTION

Ferromagnetic semiconductors (FMS) have been a subject of large scientific interest for more than two decades, since their development is of major importance for future semiconductor spintronics [1,2]. Complex FMS are a new way to solve the semiconductor spintronics problem since they offer several advantages over the widely known and intensively studied Mn-alloyed II-VI, III-V, and IV-VI compound semiconductors. Up until now, the past few decades of technological development of III-V and IV-VI FMS have led to the presence of ferromagnetism in $Ga_{1-x}Mn_xAs$ and $Ge_{1-x}Mn_xTe$ with the Curie temperature T_C with values not exceeding 200 K [3]. It is therefore important that at present there exist no homogeneous FMS showing room-temperature ferromagnetism. It creates an increasing interest in nanocomposite FMS, consisting of ferromagnetic clusters of micrometer or nanometer size, embedded into the semiconductor matrix. Such systems are expected to provide the solution to the semiconductor spintronics challenge.

Complex FMS based on semiconducting Mn-alloyed chalcopyrite II-IV-V_2 materials recently attracted significant scientific interest due to the presence of room-temperature ferromagnetic order observed in several materials [4,5]. The presence of micrometer- or nanometer-size magnetic clusters with dominant short-range magnetic interactions leading to ferromagnetism is responsible for room-temperature ferromagnetic order in several II-IV-V_2 alloys such as $ZnGeAs_2$+MnAs with T_C reaching 320 K [6], $CdGeAs_2$+MnAs with maximum T_C of about 333 K [7], and many others. The progress in the development and understanding of the properties of nanocomposite II-IV-V_2 alloys has led to the optimization of self-organization of ferromagnetic nanoclusters achieved recently in the $ZnSnAs_2$+MnAs composite [8]. The possibility of self-organization of clusters in a semiconductor matrix will possibly lead to gaining control of the magnetotransport and magnetic parameters of nanocomposites. It is very important to gain precise control of the correlation between the structural parameters and magnetic and magnetotransport properties of II-IV-V_2+MnAs nanocomposite materials. In particular, crucial from the point of view of potential applications is to gain control over the giant and colossal magnetoresistance effects observed in a variety of II-IV-V_2 materials [9]. Moreover, II-IV-V_2 materials such as $CdSnAs_2$ under a strain causing a 7% decrease in the lattice constant will become a three-dimensional topological insulator [10]. A number of interesting quantum effects have been predicted when the surface states are influenced by the magnetic impurities [11]. That could open up new opportunities for applications of II-IV-V_2 materials in spintronics.

The present paper is focused on the studies of the structural, magnetic, and magnetotransport properties of $Cd_{1-x-y}Mn_xZn_ySnAs_2$ crystals with the average Mn content x changing from 0 to 0.170 and Zn content y varying from 0.002 to 0.051. We study the limits of Mn alloying, at which this material is either an homogeneous alloy or composite with ferromagnetic clusters. We will also study the influence of the Mn alloying on the magnetotransport properties of this material.

II. SAMPLE PREPARATION

Crystals $(Cd_{1-x_t}Zn_{x_t}Sn)_{1-y_t}Mn_{y_t}As_2$ with the technological Zn chemical content x_t nominally ranging from 0 to 0.01 and technological Mn chemical content y_t ranging from 0.025 to 0.05 were grown by the horizontal Bridgman method. The starting polycrystalline materials were prepared from 99.999%–99.9999% pure elemental Cd, Zn, Mn, Sn, and As.

---

[*] kilan@ifpan.edu.pl

Arsenic pieces were additionally purified in a Br-methanol solution to avoid As_2O_3 contamination. The doping Mn was added in the form of arsenide, MnAs. Prior to single-crystal growth, the syntheses of SnAs and $(Cd_{1\text{-}x_t}Zn_{x_t})_3As_2$ were carried out by heating stoichiometric mixtures of elements above the melting point to 640 °C and 750 °C, respectively. To decrease the quantity of the excess gases, the syntheses by melting were conducted in heavily charged quartz ampoules. Ampoules were annealed at 1000 °C and sealed under vacuum of 10^{-3} Pa. The synthesis of MnAs was done from the vapor at temperature gradient 600–700 °C due to the high-temperature melting point of manganese arsenides (above 935 °C), high melting point of Mn (1244 °C), and low boiling point of pure As (615 °C). The obtained binary/ternary compounds were ground to a fine powder and mixed in stoichiometric ratio. The melt was homogenized in a horizontal furnace for three days at 740 °C followed by the temperature lowering to 640 °C. Unseeded (nucleation in conical end of ampoule) growth procedure was applied. Ampoule was pulled through a temperature gradient of 200 °C/5 cm at a rate of 2 mm/h. Due to directional solidification, the segregation resulted in a nonuniform distribution of doping elements. To study the doping possibilities and dopant segregation effect, the crystals were cut into slices perpendicular to the growth direction. The surface of the samples was polished prior to the basic structural characterization.

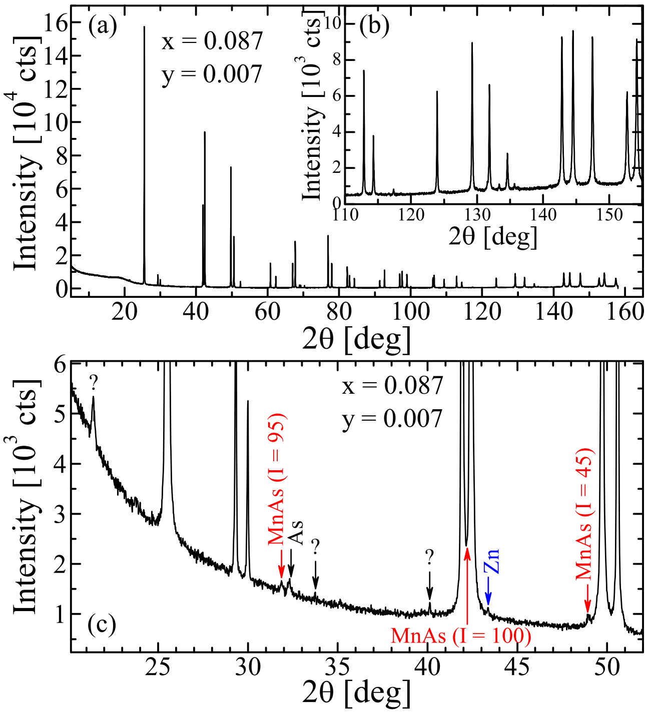

FIG. 1. X-ray diffraction patterns obtained for the representative $Cd_{1\text{-}x\text{-}y}Mn_xZn_ySnAs_2$ sample with $x = 0.087$ and $y = 0.007$. (a) Full range of 2θ angles, (b) magnified high-angle part of this pattern, and (c) magnification of the part of pattern in which reflections from foreign phases were observed.

III. STRUCTURAL CHARACTERIZATION

The chemical composition of the as-grown $Cd_{1\text{-}x\text{-}y}Mn_xZn_ySnAs_2$ crystal slices was studied with the use of the energy-dispersive x-ray fluorescence (EDXRF) method. The measurements were done with the use of the Tracor X-ray Spectrace 5000 EDXRF spectrometer. The maximum relative error of the EDXRF technique does not exceed 10% of the calculated values of the Mn and Zn contents, x and y, respectively. As a result of the EDXRF measurements, we obtained molar fractions of each element in the studied alloy. The obtained molar fractions indicate, within the accuracy of the EDXRF method, the correct stoichiometry of our samples. The results of the EDXRF measurements indicate that our samples have a broad range of Mn contents x, ranging from 0.013 up to 0.17, and Zn contents y, ranging from 0.002 up to 0.051.

The phase analysis, crystal quality, and the lattice parameters of a few selected $Cd_{1\text{-}x\text{-}y}Mn_xZn_ySnAs_2$ crystals were determined with the use of the powder x-ray diffraction (HRXRD) method. Measurements were performed using the multipurpose high-resolution X'Pert MPD Pro Alpha1, Panalytical diffractometer with Cu $K_{\alpha 1}$ radiation ($\lambda = 1.540\,598$ Å). In this instrument, the classical Bragg-Brentano geometry is modified through installation of the Johansson Ge(111) monochromator in the incident beam and a linear semiconductor strip detector. The HRXRD patterns were collected during 20 h each in the 5 to 160 2θ range. Because of a high sensitivity of the diffractometer, reflections of intensity as low as 0.06% could be detected. The measured patterns were next analyzed using the numerical procedure of SCANIX 2.60PC [12]. This procedure allows to determine the crystal system and Bravais lattice and to calculate the unit-cell parameters with high accuracy. The x-ray diffraction pattern for the $Cd_{1\text{-}x\text{-}y}Mn_xZn_ySnAs_2$ sample with composition $x = 0.087$ and $y = 0.007$ is shown in Fig. 1. The analysis of this pattern showed that almost all of the diffraction lines (with the exception of a few very weak ones) originate from this sample. Phase analysis confirmed that the studied sample crystallizes in the chalcopyrite phase with a tetragonal symmetry group of $I\text{-}42d$, similarly to the pure $CdSnAs_2$ compound. The lattice parameters of pure $CdSnAs_2$ are $a = 6.0920$ Å and $c = 11.9200$ Å [Joint Committee on Powder Diffraction Standards (JCPDS) card number 72-1239] or $a = 6.0938(1)$ Å and $c = 11.9202(2)$ Å (on the base of our measurement). The lattice parameters of the sample with composition $x = 0.087$ and $y = 0.007$ are slightly lower than those for the pure phase and are as follows: $a = 6.0912(1)$ Å and $c = 11.9167(3)$ Å. We obtained a very similar result for the sample with composition $x = 0.170$ and $y = 0.002$: $a = 6.09125(1)$ Å and $c = 11.9165(2)$ Å. It means that in both cases, we have the $Cd_{1\text{-}x\text{-}y}Mn_xZn_ySnAs_2$ alloy with x much smaller than 0.087. The remaining part of Mn exists inside the samples in the form of MnAs precipitates with different dimensions of crystallites. In both samples, we identified trace amounts of the hexagonal MnAs phase with lattice parameters $a = 3.72$ Å, $c = 5.71$ Å (JCPDS 28-0644), as well as the rhombohedral As (JCPDS 05-0632) and hexagonal Zn (JCPDS 04-0831), respectively [see Fig. 1(c)]. Moreover, as it is seen in Fig. 2, most of the MnAs phase exists inside the samples in the form of nanocrystalline precipitates with

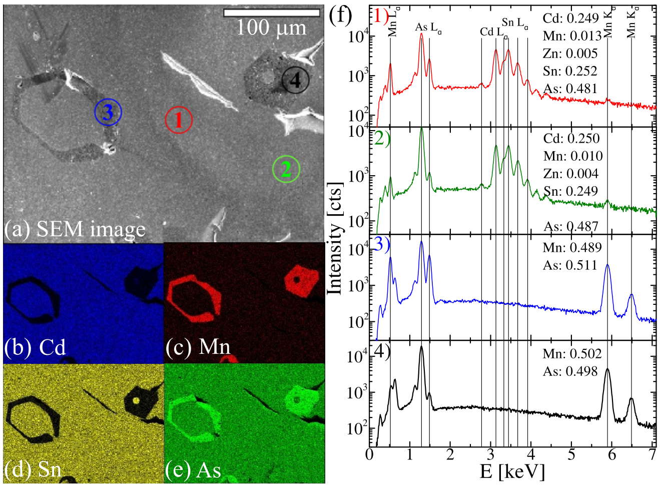

FIG. 2. Results of the SEM/EDX measurements obtained at room temperature for the representative $\mathrm{Cd}_{1\text{-}x\text{-}y}\mathrm{Mn}_x\mathrm{Zn}_y\mathrm{SnAs}_2$ sample with $x = 0.087$ and $y = 0.007$ including the following: (a) SEM image and (b)–(f) EDX microprobe results, including (b)–(e) maps of the distribution of the alloying elements and (f) the results of detailed chemical-content measurements done at different spots [marked as numbers in (a)] of the sample surface.

dimensions that are too small for detection by the x-ray diffraction.

The chemical-composition homogeneity of our $\mathrm{Cd}_{1\text{-}x\text{-}y}\mathrm{Mn}_x\mathrm{Zn}_y\mathrm{SnAs}_2$ crystals was studied with the use of the Hitachi SU-70 Analytical UHR FE-SEM scanning electron microscope (SEM) coupled with Thermo Fisher NSS energy-dispersive x-ray spectrometer system (EDS) equipped with a silicon drift detector. A few $\mathrm{Cd}_{1\text{-}x\text{-}y}\mathrm{Mn}_x\mathrm{Zn}_y\mathrm{SnAs}_2$ samples, having different chemical compositions, were polished and chemically cleaned prior to the SEM/EDS measurements. A series of high-resolution images of the crystal surface was done at different sample spots and magnifications. The SEM measurements reveal the presence of micrometer-size inhomogeneities in the $\mathrm{Cd}_{1\text{-}x\text{-}y}\mathrm{Mn}_x\mathrm{Zn}_y\mathrm{SnAs}_2$ samples with the Mn contents, $x \geqslant 0.076$ [see Fig. 2(a)]. The detailed SEM measurements reveal that for our samples with $x \geqslant 0.076$, the presence of clusters randomly distributed in the host $\mathrm{Cd}_{1\text{-}x\text{-}y}\mathrm{Mn}_x\mathrm{Zn}_y\mathrm{SnAs}_2$ lattice is observed, while for the samples with $x \leqslant 0.025$, inhomogeneities are not observed. The sizes of the clusters are broadly distributed, ranging from 100 up to about 200 μm. The EDX spectra taken from the area of the $\mathrm{Cd}_{1\text{-}x\text{-}y}\mathrm{Mn}_x\mathrm{Zn}_y\mathrm{SnAs}_2$ lattice show a correct stoichiometry of the alloy and the presence of a small quantity of Mn (maximum of about $x \approx 0.01$), most probably randomly distributed in the host lattice. This result indicates that the Mn solubility in the CdSnAs_2 lattice is around 1 mol%. This result corresponds well to the HRXRD results, which show the presence of precipitations associated with Mn ions for the samples with $x \geqslant 0.076$. Our SEM/EDX measurements did not show any signatures of Zn clustering in our samples. Moreover, Zn is visible in the host $\mathrm{Cd}_{1\text{-}x\text{-}y}\mathrm{Mn}_x\mathrm{Zn}_y\mathrm{SnAs}_2$ lattice in quantities similar to the average y values measured with the EDXRF method.

IV. MAGNETIC IONS IN THE SEMICONDUCTOR LATTICE

Magnetic properties of our $\mathrm{Cd}_{1\text{-}x\text{-}y}\mathrm{Mn}_x\mathrm{Zn}_y\mathrm{SnAs}_2$ samples were studied with the use of three magnetometers, allowing the measurements of the dynamic magnetic susceptibility χ_{AC}, and static magnetization M as a function of the magnetic field B and temperature T. The low-field magnetization measurements were performed with the use of the vibrating sample magnetometer (VSM) system and the Quantum Design XL-5 Magnetic Property Measurement System equipped with a superconducting quantum interference device (SQUID). The measurements of the ac magnetic susceptibility and the high-field static magnetization were performed with the use of the LakeShore 7229 AC Susceptometer/DC Magnetometer system.

At first, the detailed measurements of dynamic magnetic susceptibility over the temperature range from 4.3 up to 320 K were performed. During the measurements, the sample was put into the alternating magnetic field with the frequency f equal to 625 Hz and amplitude $H_{AC} = 10$ Oe. As a result, we obtained a series of temperature dependencies of both real and imaginary parts of the ac susceptibility, $\mathrm{Re}(\chi_{AC})$ and $\mathrm{Im}(\chi_{AC})$, respectively. The measurements done on all of our $\mathrm{Cd}_{1\text{-}x\text{-}y}\mathrm{Mn}_x\mathrm{Zn}_y\mathrm{SnAs}_2$ crystals indicated a vanishing imaginary part of the ac magnetic susceptibility. The temperature dependence of the real part of the ac magnetic susceptibility for selected $\mathrm{Cd}_{1\text{-}x\text{-}y}\mathrm{Mn}_x\mathrm{Zn}_y\mathrm{SnAs}_2$ samples is presented in Fig. 3. The $\mathrm{Re}(\chi_{AC})(T)$ curves obtained at temperatures $T \leqslant 320$ K show positive $\mathrm{Re}(\chi_{AC})$ values with large changes as a function of temperature. For $\mathrm{Cd}_{1\text{-}x\text{-}y}\mathrm{Mn}_x\mathrm{Zn}_y\mathrm{SnAs}_2$ samples with $x \geqslant 0.076$ at temperatures from about 300 to 310 K, a rapid decrease $\mathrm{Re}(\chi_{AC})(T)$ with increasing T is observed. It is a signature of a presence of a magnetic transition in these samples. Similar behavior is known for ZnGeAs_2+MnAs

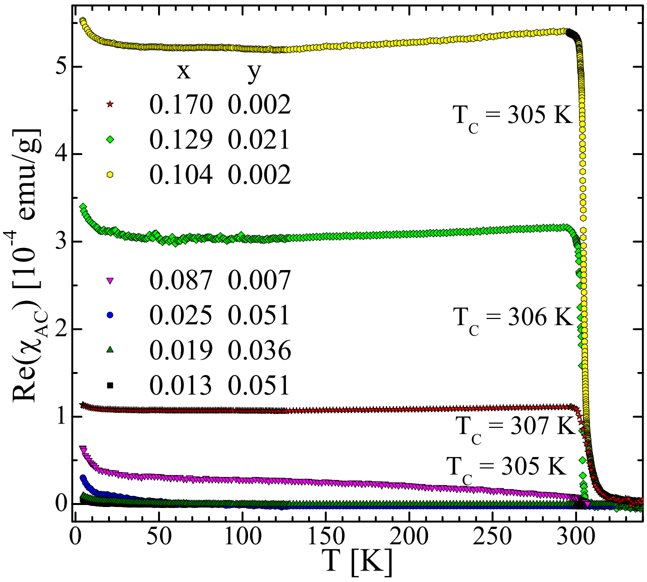

FIG. 3. Temperature dependence of the real part of the ac magnetic susceptibility obtained for the selected $\mathrm{Cd}_{1\text{-}x\text{-}y}\mathrm{Mn}_x\mathrm{Zn}_y\mathrm{SnAs}_2$ samples with different average Mn and Zn contents x and y, respectively.

TABLE I. Parameters obtained from the magnetometric studies of the $Cd_{1-x-y}Mn_xZn_ySnAs_2$ crystals with different chemical compositions, x and y, including: the Curie temperature T_C, the Curie-Weiss temperature θ, the Curie constant C, the active Mn content x_θ, calculated from the Curie constant using Eq. (2), the saturation magnetization M_S, and the active Mn content x_m, calculated from the saturation magnetization using Eq. (3).

$x \pm \Delta x$	$y \pm \Delta y$	$T_C \pm \Delta T_C$ (K)	$C \pm \Delta C$ (10^{-4}) (emu K/g)	$x_\theta \pm \Delta x_\theta$	$\theta \pm \Delta\theta$ (K)	$M_S \pm \Delta M_S$ (emu/g)	$x_m \pm \Delta x_m$
0.013 ± 0.001	0.051 ± 0.005		0.27 ± 0.02	0.002 ± 0.0002	0.03 ± 0.01	0.18 ± 0.02	0.0024 ± 0.0002
0.019 ± 0.002	0.036 ± 0.004		0.49 ± 0.04	0.004 ± 0.0004	0.05 ± 0.01	0.41 ± 0.04	0.0056 ± 0.0005
0.025 ± 0.002	0.028 ± 0.028		1.7 ± 0.1	0.015 ± 0.001	−0.9 ± 0.1	1.2 ± 0.1	0.016 ± 0.002
0.076 ± 0.007	0.004 ± 0.001	304 ± 1	2.2 ± 0.3	0.019 ± 0.002	304 ± 2	1.4 ± 0.1	0.019 ± 0.002
0.087 ± 0.008	0.007 ± 0.001	305 ± 1	2.9 ± 0.5	0.026 ± 0.004	305 ± 2	1.6 ± 0.1	0.022 ± 0.003
0.104 ± 0.010	0.002 ± 0.001	305 ± 1	5.8 ± 0.6	0.051 ± 0.005	306 ± 2	2.9 ± 0.1	0.039 ± 0.004
0.129 ± 0.012	0.027 ± 0.002	306 ± 1	7.6 ± 0.8	0.068 ± 0.007	304 ± 1	4.3 ± 0.2	0.057 ± 0.006
0.170 ± 0.017	0.002 ± 0.001	307 ± 1	9.4 ± 0.7	0.084 ± 0.006	307 ± 2	6.2 ± 0.2	0.082 ± 0.008

[6] and $CdGeAs_2$+MnAs [7] systems showing ferromagnetic order with the Curie temperature T_C around 320 K. We assign this transition to be related to the presence of MnAs clusters embedded in the $Cd_{1-x-y}Mn_xZn_ySnAs_2$ lattice.

The Curie temperature of the ferromagnetic samples can be estimated from $\mathrm{Re}(\chi_{AC})(T)$ dependence as a point where $\partial^2\mathrm{Re}(\chi_{AC})/\partial T^2 = 0$. The estimated Curie temperatures for our samples are given in Table I. The obtained T_C values do not change as a function of the Mn contents x. Our samples show T_C value in the range from 304 to 306 K, and are slightly lower than the values observed in the literature for the $ZnGeAs_2$+MnAs [6] and $CdGeAs_2$+MnAs [7] systems. Our samples, in similarity to the binary counterpart of II-IV-V_2 compounds, namely III-V compound GaAs with MnAs clusters, show similar magnetic transition near room temperature [13]. There have also been many studies of methods to control the structural and geometrical properties of nanoclusters [14,15]. It is therefore possible that the geometrical and chemical parameters of the clusters are responsible for slightly lower T_C values observed in our $Cd_{1-x-y}Mn_xZn_ySnAs_2$ crystals with $x \geqslant 0.076$ with respect to other known II-IV-V_2+MnAs systems.

At temperatures lower than 50 K, a small increase of $\mathrm{Re}(\chi_{AC})(T)$ with decreasing T is observed, indicating a paramagnetic contribution to the total magnetic susceptibility, $\mathrm{Re}(\chi_{AC})$. This contribution at low temperatures is dominant over the signal from ferromagnetic MnAs clusters. This means that Mn is incorporated into the $Cd_{1-y}Zn_ySnAs_2$ semiconductor lattice to a significant percentage. This result is consistent with the previous results of SEM/EDX measurements, indicating that a significant fraction of all the Mn ions introduced in the crystals during synthesis is distributed randomly in the semiconductor crystal lattice. This result is similar to other II-IV-V_2 group representatives such as $Zn_{1-x}Mn_xGeAs_2$ [16] or $Cd_{1-x}Mn_xGeAs_2$ [17] in which the solubility of Mn is of the order of few molar percent.

The magnetic behavior of our $Cd_{1-x-y}Mn_xZn_ySnAs_2$ samples has a strong influence on their transport properties. The temperature dependence of the resistivity, $\rho_{xx}(T)$, was measured for all of our samples over the temperature range from $T \approx 1.6$ K up to 380 K. The representative results for the samples with different chemical compositions, x and y, are presented in Fig. 4. Two physical effects influence the shape of the $\rho_{xx}(T)$ curves. At first, all of our samples show an increase of the resistivity with an increasing temperature. It is a feature typical of a semimetal or degenerate semiconductor. All of our samples belong to degenerate semiconductors. The second interesting effect was observed only for our ferromagnetic $Cd_{1-x-y}Mn_xZn_ySnAs_2$ samples with $x \geqslant 0.076$. At temperatures close to T_C, a peak in the $\rho_{xx}(T)$ curves is observed. A similar peak was also reported in the literature for composite $ZnGeAs_2$+MnAs samples [6]. The appearance of the peak in the resistivity at a temperature close to the phase transition is related with the scattering of carriers at the magnetization fluctuations near the Curie temperature [18].

The dc magnetometery was used to complement the ac magnetic susceptibility studies. A series of dc magnetization measurements was performed in the range of low magnetic field $B \leqslant 50$ mT using the VSM and SQUID magnetometers. Measurements were done over a wide temperature range, $T = 295$–600 K. During the measurements, the sample was

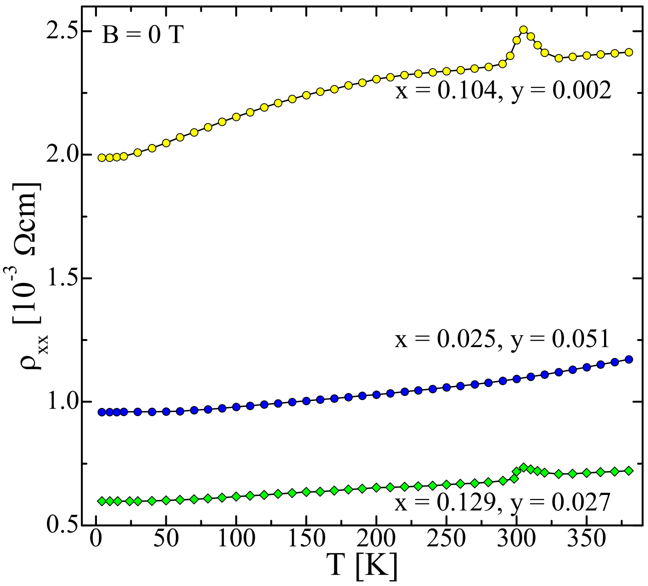

FIG. 4. Temperature dependence of the resistivity, ρ_{xx}, obtained for the selected $Cd_{1-x-y}Mn_xZn_ySnAs_2$ samples with different Mn and Zn contents, x and y.

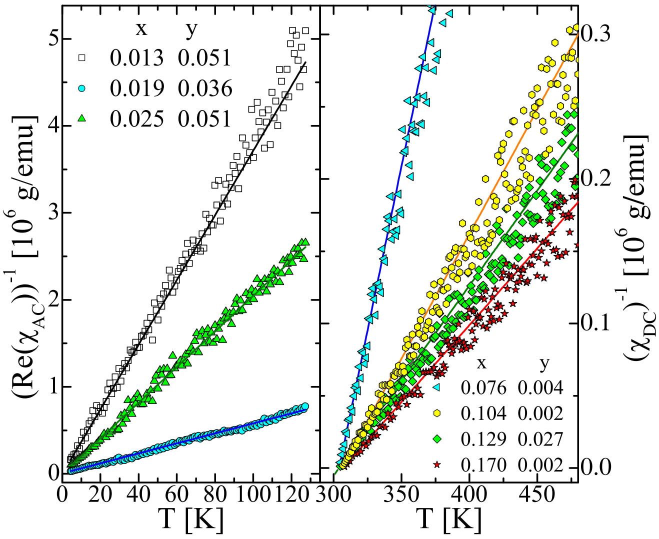

FIG. 5. Temperature dependence of the inverse of the ac and dc magnetic susceptibility obtained for the selected $\mathrm{Cd}_{1\text{-}x\text{-}y}\mathrm{Mn}_x\mathrm{Zn}_y\mathrm{SnAs}_2$ samples with different Mn and Zn contents, x and y (markers), and fitted to the Curie-Weiss law with Eq. (1) (lines).

cooled in the the absence of the external magnetic field. The contribution to the total magnetization, related to the sample holder, was removed from the experimental results. Our results indicate that up to 50 mT, the isothermal magnetization $M(B)$ curves at temperatures higher than 320 K, e.g., in the paramagnetic region, were nearly linear, allowing us to calculate the dc magnetic susceptibility, $\chi_{DC} = \partial M/\partial B$, and its changes with temperature for each of our $\mathrm{Cd}_{1\text{-}x\text{-}y}\mathrm{Mn}_x\mathrm{Zn}_y\mathrm{SnAs}_2$ samples. Our results indicate that for all of the studied samples, $\chi_{DC}(T = 300\ \mathrm{K}) = \mathrm{Re}(\chi_{AC})(T = 300\ \mathrm{K})$, allowing interchangeable use of these quantities. The results of our calculations in the form of temperature dependencies of the inverse of the ac and dc magnetic susceptibility, $[\mathrm{Re}(\chi_{AC})]^{-1}$ and $(\chi_{DC})^{-1}$, respectively, for selected samples are presented in Fig. 5. The temperature dependence of the ac and dc magnetic susceptibility at temperatures well above T_C for our $\mathrm{Cd}_{1\text{-}x\text{-}y}\mathrm{Mn}_x\mathrm{Zn}_y\mathrm{SnAs}_2$ samples can be described with the use of the modified Curie-Weiss law,

$$\chi = \frac{C}{T-\theta} + \chi_{\mathrm{dia}}, \tag{1}$$

with the Curie constant C prescribed as

$$C = \frac{N_0 g^2 \mu_B^2 S(S+1) x_\theta}{3k_B}, \tag{2}$$

where θ is the paramagnetic Curie-Weiss temperature, N_0 is the number of cation sites per gram, g is the effective spin splitting factor (for Mn ions, $g \approx 2$), S is the spin number of Mn (for Mn^{2+}, $S = 5/2$), μ_B is the Bohr magneton, x_θ is the content of the magnetically active Mn ions, k_B is the Boltzmann constant, and χ_{dia} is the diamagnetic susceptibility of the nonmagnetic CdSnAs_2 host crystal. The inverse of the ac and dc magnetic susceptibility (presented in Fig. 5) at temperatures well above T_C, i.e., in a paramagnetic region, show a nearly linear temperature dependence according to the modified Curie-Weiss law. It allowed fitting of the experimental results to the Curie-Weiss law [Eq. (1)]. We fitted the results obtained over the temperature range from 100 to 300 K for the paramagnetic samples with $x \leqslant 0.025$ and over the temperature range from 400 to 600 K for the ferromagnetic samples with $x \geqslant 0.076$. For the fitting procedure, we used the constant value of the diamagnetic contribution to the dc magnetic susceptibility. For the purposes of proper magnetometric data analysis, we measured the magnetic susceptibility for a small pure CdSnAs_2 sample. The estimated χ_{dia} value for CdSnAs_2 lattice equals -2×10^{-7} emu/g. The estimated χ_{dia} value is similar to that for ZnGeAs_2 equal to -2×10^{-7} emu/g [16] and for CdGeAs_2 equal to -2.5×10^{-7} emu/g [17]. The experimental $\mathrm{Re}(\chi_{AC})(T)$ and $\chi_{DC}(T)$ curves were fitted with only two fitting parameters: the Curie constant C and the Curie-Weiss temperature θ. The fitted lines are presented together with the experimental data in Fig. 5. The fitting procedure showed that the magnetic susceptibility of our samples can be very well fitted with the use of the Curie-Weiss law described with Eq. (1) at temperatures higher than T_C by about 100 K. As a result of the fitting procedure, we obtained the values of two parameters, C and θ, gathered for all our samples in Table I. The obtained C values can be further used to calculate the amount of magnetically active Mn ions, x_θ, from Eq. (2). The calculated x_θ values are shown in Table I.

As we can see in Table I, for all of our $\mathrm{Cd}_{1\text{-}x\text{-}y}\mathrm{Mn}_x\mathrm{Zn}_y\mathrm{SnAs}_2$ samples, $x_\theta < x$. There is a possible interpretation of the $x_\theta < x$, observed for all of our samples. A large fraction of the Mn ions allocated in our $\mathrm{Cd}_{1\text{-}x\text{-}y}\mathrm{Mn}_x\mathrm{Zn}_y\mathrm{SnAs}_2$ samples can have a charge state different from the Mn^{2+}, which is a high-spin state for Mn with the total magnetic momentum J equal to $J = S = 5/2$. The results of fitting might also be influenced by the application of the modified Curie-Weiss law at temperatures too close to T_C for the samples with $x \geqslant 0.076$. Due to the risk of the sample annealing and because of experimental limitations, it was not possible and reasonable to measure magnetic properties of the samples at $T > 600$ K. It is then possible that in the temperature range from 350 to 600 K for the ferromagnetic samples with $x \geqslant 0.076$ and at low magnetic field $B < 50$ mT used for the calculation of the experimental $\chi_{DC}(T)$ curves, not all of the Mn magnetic moments in our samples are paramagnetic. This could lead to the underestimation of the x_θ values.

The Curie-Weiss temperatures θ obtained during the fitting procedure have values close to 0 for the paramagnetic, homogeneous $\mathrm{Cd}_{1\text{-}x\text{-}y}\mathrm{Mn}_x\mathrm{Zn}_y\mathrm{SnAs}_2$ samples with $x \leqslant 0.025$. It is a signature that most of the Mn ions in these samples do not interact and can be treated as isolated magnetic moments. For the ferromagnetic, composite samples with $x \geqslant 0.076$, the Curie-Weiss temperature has values close to 305 K, e.g., close to T_C. It is a signature that the Mn ions in MnAs clusters present in these samples interact ferromagnetically and the role of magnetic disorder in this material is rather small.

We performed a series of measurements of the magnetic field dependencies of the magnetization at several stabilized temperatures for all of our $\mathrm{Cd}_{1\text{-}x\text{-}y}\mathrm{Mn}_x\mathrm{Zn}_y\mathrm{SnAs}_2$ samples with different chemical compositions, x and y. The magnetization $M(B)$ was measured using two different magnetometer systems because of temperature and magnetic field limitations

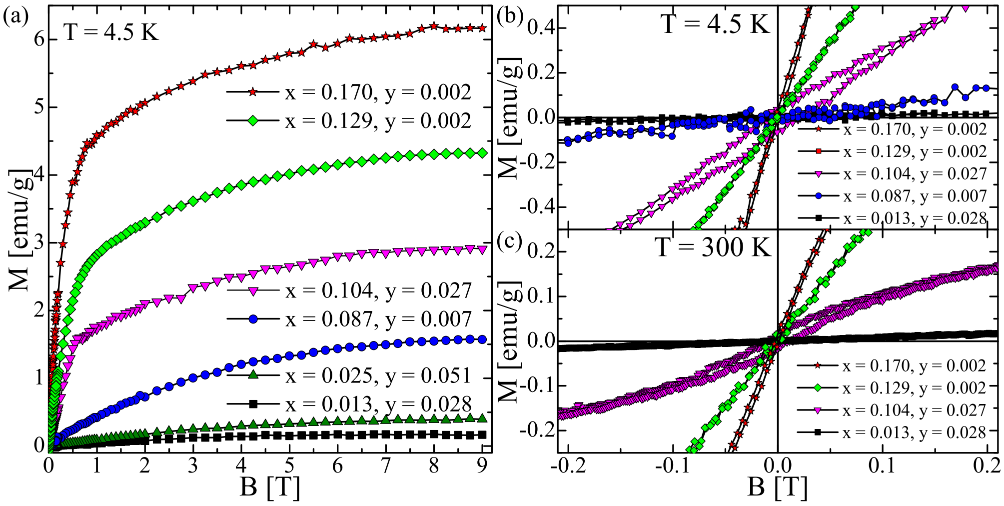

FIG. 6. Results of the isothermal magnetization studies for the selected $Cd_{1\text{-}x\text{-}y}Mn_xZn_ySnAs_2$ samples with different Mn and Zn contents, x and y, including: (a) magnetization as a function of the applied static magnetic field at $T = 4.5$ K, (b),(c) magnetization hysteresis curves measured at (b) $T = 4.5$ K and (c) $T = 300$ K.

of both used setups. We used two magnetometers to cover the large temperature range where the samples show ferromagnetic order. At temperatures lower than $T = 200$ K, the magnetization $M(B)$ curves were measured using the the LakeShore 7229 magnetometer system using the Weiss extraction method and equipped with a superconducting coil allowing the measurements at constant magnetic fields up to $B = 9$ T. At $T \approx 300$ K, the magnetization curves were measured with the use of the VSM system, allowing us to produce constant magnetic field up to $B = 1.5$ T. All of the obtained raw experimental results were corrected by subtracting the contribution of the sample holder from the total magnetic moment. The $M(B)$ curves measured at low temperatures and up to high magnetic field values carry the most information about the magnetic ions in the material. Moreover, for clarity of data presentation, the results obtained at the lowest temperature, $T = 4.5$ K, and at room temperature are presented. The magnetization $M(B)$ curves obtained at $T = 4.5$ K for the selected $Cd_{1\text{-}x\text{-}y}Mn_xZn_ySnAs_2$ samples with different chemical compositions, x and y, are presented in Fig. 6. As expected, the shapes of the $M(B)$ curves obtained at $T = 4.5$ K differ for the paramagnetic ($x \leqslant 0.025$) and ferromagnetic ($x \geqslant 0.076$) samples. For the paramagnetic samples with $x \leqslant 0.025$, the $M(B)$ curves at $T = 4.5$ K show saturation and the Brillouin-like shape. At higher temperatures, as expected for a paramagnetic material, the saturation of $M(B)$ curves is no longer observed. For the ferromagnetic samples with $x \geqslant 0.076$, the $M(B)$ curves at $T < T_C$ have a similar shape (like at $T = 4.5$ K) and do not change much with temperature.

The $M(B)$ curves obtained at $T = 4.5$ K are Brillouin-like functions with magnetization saturation at $B > 8$ T, allowing us to estimate the saturation magnetization M_S for each of our samples. The diamagnetic contribution to M originating from the host lattice, with the value equal to $\chi_{\text{dia}} = -2 \times 10^{-7}$ emu/g, was subtracted from the total magnetization for the purpose of the proper estimation of M_S. The obtained M_S values are gathered for all studied samples in Table I. As expected, the M_S values increase as a function of the Mn content x.

The saturation magnetization of the system with magnetic impurities can be described with the use of the following equation:

$$M_S = x_m N_0 \mu_B g S, \tag{3}$$

where x_m is the effective content of magnetically active Mn. The obtained values of x_m, gathered in Table I, show that $x_m \approx x_\theta$ within the limits of the error in the determination of both quantities. It is a signature that the analysis of the magnetic susceptibility curves based on the modified Curie-Weiss law gave reliable results. It is also a proof that the conclusions drawn from the obtained x_θ values are correct.

The detailed measurements of the magnetization hysteresis curves were done for all our $Cd_{1\text{-}x\text{-}y}Mn_xZn_ySnAs_2$ samples at temperatures below 400 K. Representative magnetization hysteresis curves obtained at $T = 4.5$ K and 300 K are presented in Figs. 6(b) and 6(c). Irreversible behavior of the magnetization $M(B)$ curves was observed only for the samples with $x \geqslant 0.076$, e.g., for the composite ferromagnetic samples with MnAs clusters. For the ferromagnetic samples with $x \geqslant 0.076$, narrow magnetization hysteresis loops were observed at temperatures below T_C. The parameters characterizing magnetization hysteresis loops as well as their shapes do not show large changes with increasing temperature from $T = 4.5$ K up to T_C, where the hysteresis loop is no longer observable. The coercive field B_C and remanent magnetization M_R estimated from the magnetization hysteresis loops have low values [see Figs. 6(b) and 6(c)] for most of the studied samples, except for the sample with $x = 0.104$ and $y = 0.027$, where the coercive field B_C equals about 250 Gs at $T = 4.5$ K, slowly decreases to about 100 Oe at room temperature, and vanishes at $T > T_C$. The change of the coercive field with x is most probably related to the microscopic properties of the clusters domain size change.

V. TRANSPORT AND MAGNETOTRANSPORT PROPERTIES

The studies of electrical transport and magnetotransport properties of the $\text{Cd}_{1\text{-}x\text{-}y}\text{Mn}_x\text{Zn}_y\text{SnAs}_2$ crystals included the measurements of the the magnetoresistance and the Hall effect. The obtained data were used to calculate the resistivity tensor components, ρ_{xx} and ρ_{xy}. The measurements were carried out with the use of two experimental setups and two different measurement procedures. We used a resistive magnet allowing the continuous change of the sample temperature from $T \approx 4$ K up to 380 K and the maximum magnetic field up to 1.5 T. The magnetotransport setup equipped with a resistive magnet was used for the Hall-effect measurements done at several stabilized temperatures and selected stabilized magnetic field values in order to obtain precise values of the resistivity tensor component ρ_{xx}, the Hall carrier concentration n, and the Hall carrier mobility μ for each of the studied samples. In addition to the low-field magnetotransport measurements, we performed measurements with the use of the superconducting magnet with the maximum magnetic field equal to $B = 13$ T. The measurements of the magnetic field dependence of the resistivity components, ρ_{xx} and ρ_{xy}, were done with the magnetic field continuously swept between ± 13 T with a sweep speed not exceeding about 0.5 T/min. The magnetotransport setup with the superconducting magnet was equipped with the cryostat allowing the control of the temperature of the sample from 1.4 up to 300 K. The samples, cut to the size of about $1 \times 1 \times 8$ mm, were etched, polished, and cleaned prior to making electrical contacts. The contacts were made with the use of an indium solder and gold wires. The ohmic behavior of the prepared contacts was checked prior to proper measurements. Both $\rho_{xx}(B)$ and $\rho_{xy}(B)$ dependencies were measured simultaneously at dozens of selected stabilized temperatures.

Initially, we measured the temperature dependence of the resistivity ρ_{xx} at $B = 0$ T and the Hall effect up to $B = 1.5$ T for all of our samples. The selected results of the low-field magnetotransport measurements obtained at $T = 4.3$ K and 300 K are gathered in Table II. The resistivity values measured at $T = 300$ K (see Table II) do not show a monotonic trend as a function of the chemical contents, x and y. More detailed observations can be made upon the analysis of the Hall-effect data.

The low-field magnetotransport studies of our $\text{Cd}_{1\text{-}x\text{-}y}\text{Mn}_x\text{Zn}_y\text{SnAs}_2$ samples were done in order to precisely measure the temperature dependencies of the Hall carrier concentration n and the Hall carrier mobility μ for each of our crystals. The magnetic field dependence of the Hall resistivity tensor component, ρ_{xy}, is linear as a function of the applied magnetic field in the entire studied temperature range (no anomalous Hall-effect contribution was observed). This allows precise and simple calculation of the Hall carrier concentration and mobility as a function of temperature. The selected values of n and μ obtained at room temperature and at liquid-helium temperature are gathered in Table II. The results indicate that all the investigated $\text{Cd}_{1\text{-}x\text{-}y}\text{Mn}_x\text{Zn}_y\text{SnAs}_2$ crystals are n-type semiconductors. For all of our samples, the Hall carrier concentration has values of the order of 1–2 $\times 10^{18}$ cm^{-3}. The temperature dependence of the Hall carrier concentration for all of our samples shows small changes of n with T, indicating that our samples are degenerate semiconductors and thermal activation of conducting carriers does not play a major role in the carrier transport in the material. The Hall carrier concentration varies with the change in the Mn content of the samples. These changes are small and not monotonic.

The Hall carrier mobility μ, estimated from the magnetotransport data using the relation $\mu = (en\rho_{xx})^{-1}$, has high values for all of our samples (see Table II). The carrier mobility does not have a clear and well-defined trend as a function of the Mn contents x. However, the general decrease of μ with x may be speculated to be related to the presence of an increasing amount of defects in materials containing large Mn contents. The highest carrier mobility value, $\mu = 7100$ cm^2/(V s), is observed for the sample with $x = 0.025$ and $y = 0.028$. The carrier mobility values, observed for our samples, are to our knowledge the highest mobility values observed for the II-IV-V$_2$ group semiconductors. For the other representatives of this group of compounds, the highest carrier mobility was reported for the $\text{Zn}_{1\text{-}x}\text{Cd}_x\text{GeAs}_2$ crystals, with the values increasing with x up to $\mu \approx 875$ cm^2/(V s) for $x = 1$ [19]. Relatively large carrier mobility $\mu = 233$ cm^2/(V s) was reported for n-type $\text{Cd}_{1\text{-}x}\text{Mn}_x\text{GeAs}_2$ crystal with 4% at. Mn [7], while for the p-type samples the reported mobility values

TABLE II. Parameters obtained from the transport and magnetotransport studies of our $\text{Cd}_{1\text{-}x\text{-}y}\text{Mn}_x\text{Zn}_y\text{SnAs}_2$ crystals with different chemical compositions, x and y: (i) low-field magnetotransport results (obtained at two temperatures $T = 4.3$ K and 300 K) including the resistivity ρ_{xx}, the Hall carrier concentration n, and the Hall carrier mobility μ, and (ii) high-field magnetotransport results including the carrier concentration n_s, the effective mass m^*, and the Dingle temperature T_D obtained from the Shubnikov–de Haas oscillation data analysis.

		ρ_{xx} (10^{-4} Ω cm)		n (10^{17} cm^{-3})		μ [cm^2/(V s)]		n_s	m^*	T_D
x	y	$T = 4.3$ K	$T = 300$ K	$T = 4.3$ K	$T = 300$ K	$T = 4.3$ K	$T = 300$ K	(10^{17} cm^{-3})	(m_e)	[K]
0.013	0.051	8.6 ± 0.1	9.6 ± 0.1	11 ± 1	11 ± 1	6550 ± 720	5940 ± 650	10 ± 1	0.112 ± 0.012	5.6 ± 0.1
0.019	0.036	8.1 ± 0.1	9.4 ± 0.1	14 ± 1	14 ± 1	5570 ± 610	4850 ± 530	12 ± 1	0.121 ± 0.012	4.8 ± 0.1
0.025	0.028	9.6 ± 0.1	11 ± 1	9.2 ± 0.1	9.2 ± 0.1	7100 ± 780	6160 ± 680	8.8 ± 0.9	0.115 ± 0.012	4.1 ± 0.1
0.076	0.004	5.7 ± 0.1	6.7 ± 0.1	16 ± 1	16 ± 1	6860 ± 750	5790 ± 640	14 ± 1	0.123 ± 0.012	7.2 ± 0.1
0.087	0.007	6.1 ± 0.1	7.1 ± 0.1	18 ± 1	18 ± 1	5650 ± 620	4860 ± 530	17 ± 2	0.121 ± 0.012	9.8 ± 0.1
0.104	0.002	20 ± 1	25 ± 1	22 ± 1	21 ± 1	1410 ± 150	1460 ± 160	18 ± 2	0.121 ± 0.012	13.6 ± 0.1
0.129	0.027	6.0 ± 0.1	7.2 ± 0.1	18 ± 1	18 ± 1	5730 ± 630	4810 ± 530	16 ± 2	0.119 ± 0.012	9.1 ± 0.1
0.170	0.002	27 ± 1	32 ± 1	19 ± 1	18 ± 1	1220 ± 130	1110 ± 120			

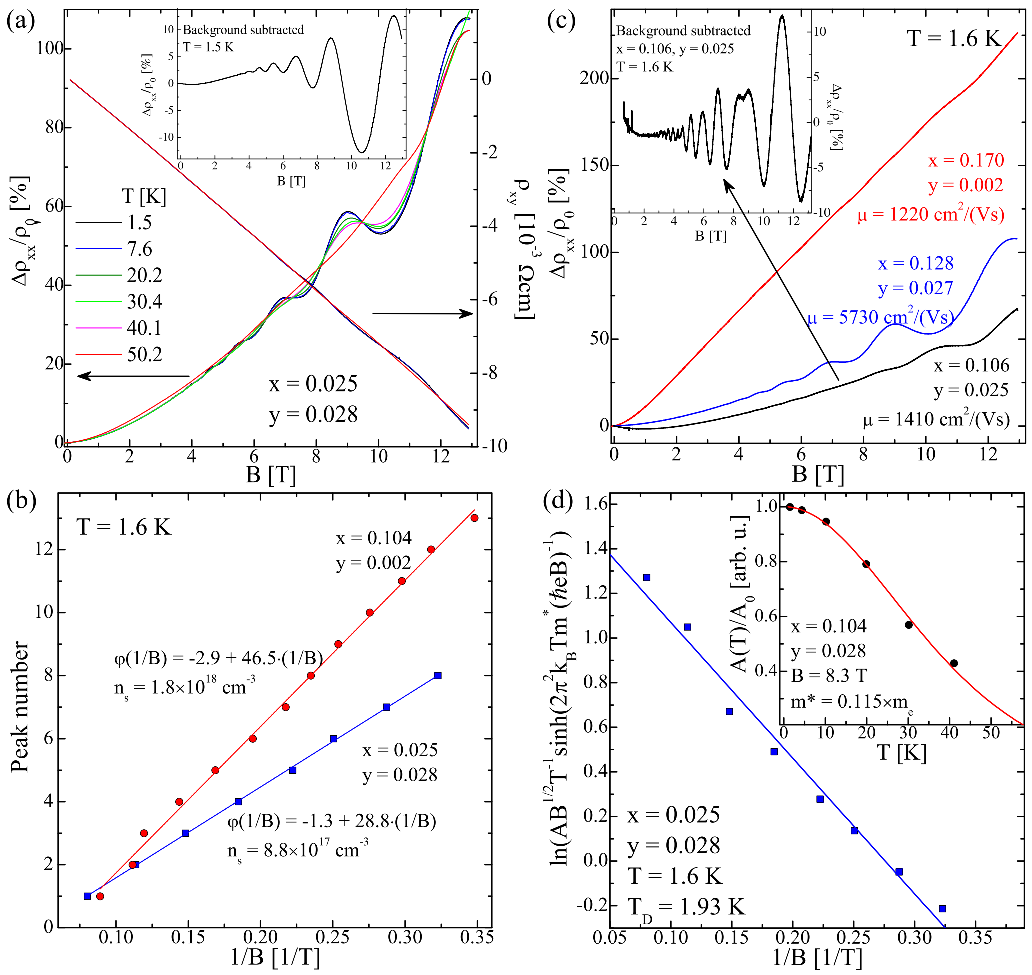

FIG. 7. Selected results of the magnetoresistance measurements obtained for our $Cd_{1-x-y}Mn_xZn_ySnAs_2$ crystals with different Mn and Zn contents, x and y, including (a) selected representative MR curves obtained for the sample with $x = 0.025$ and $y = 0.028$ (inset: SdH oscillations with quadratic contribution removed), (b) the SdH oscillation peak number vs the inverse of the magnetic field, obtained from the experimental results (symbols) and fitted with linear functions (lines) for the selected samples with different chemical contents, x and y, (c) selected typical MR curves obtained at $T \approx 1.6$ K for the samples with different chemical contents, x and y (inset: selected SdH oscillations with linear contribution removed), and (d) amplitude of the SdH oscillations, obtained experimentally for the representative sample with $x = 0.025$ and $y = 0.028$ (symbols) and fitted with the use of linear function (lines) [inset: the amplitude of the SdH oscillations as a function of temperature obtained for the sample with $x = 0.104$ and $y = 0.028$ (symbols) and fitted to Eq. (5) (line)].

were lower than 200 cm^2/(V s) [17]. The $\mu(T)$ dependence for all of our $Cd_{1-x-y}Mn_xZn_ySnAs_2$ crystals is almost constant at T changing from 4.5 to 30 K, and decreases at T from 30 to 380 K. Decreasing $\mu(T)$ observed at T increasing from 30 to 380 K is a feature characteristic of the phonon scattering mechanism. The mobility due to acoustic phonon scattering is expected to be proportional to $T^{-3/2}$, while the mobility due to optical phonon scattering is expected to be proportional to $T^{-1/2}$. The $\mu(T)$ dependence for our samples can be fitted with better convergence to $T^{-1/2}$ dependence, indicating that the optical phonon scattering is the major scattering process responsible for the observed $\mu(T)$ dependence for all of our $Cd_{1-x-y}Mn_xZn_ySnAs_2$ samples.

The high-field (up to $B = 13$ T) magnetoresistance (MR) and the Hall-effect measurements were performed for all studied samples at selected stabilized temperatures from $T = 1.4$ K up to 300 K. As a result of high-field measurements, we obtained a series of magnetic field dependencies of the resistivity tensor components, ρ_{xx} and ρ_{xy}, measured at several selected stabilized temperatures.

The Hall-effect results show the presence of plateaus in the $\rho_{xy}(B)$ curves for all of our samples at magnetic fields higher than 3 T and at temperatures lower than 50 K [see example in Fig. 7(a)]. It is a proof that the low-field Hall-effect data were analyzed correctly and the interpretation of these results is valid.

The MR curves were obtained by averaging the results for positive and negative current. For some samples and for simple data presentation, the $\rho_{xx}(B)$ curves obtained at different constant temperatures were normalized to the zero-field resistivity value $\rho_{xx}(B = 0)$ by using the following equation: $\Delta\rho_{xx}/\rho_{xx}(B = 0) = [\rho_{xx}(B) - \rho_{xx}(B = 0)]/\rho_{xx}(B = 0)$. In this way, we calculated several isothermal MR curves for most of our samples, obtained at various temperatures from the range of $1.5 < T < 300$ K. The representative, selected magnetotransport results obtained at selected stabilized temperatures for a few of our $\mathrm{Cd}_{1\text{-}x\text{-}y}\mathrm{Mn}_x\mathrm{Zn}_y\mathrm{SnAs}_2$ samples are presented in Fig. 7. The magnetotransport data gathered in Fig. 7 indicate that we can divide our samples into two groups due to the different observed magnetotransport effects.

For all of our $\mathrm{Cd}_{1\text{-}x\text{-}y}\mathrm{Mn}_x\mathrm{Zn}_y\mathrm{SnAs}_2$ samples, the Shubnikov–de Haas (SdH) oscillations are observed at $T < 50$ K [see representative MR curves in Figs. 7(a) and 7(c)]. An oscillatory character of the $\rho_{xx}(B)$ can be clearly superimposed on the parabolic dependence of the ρ_{xx} on the magnetic field for the paramagnetic samples with $x \leqslant 0.025$ [Fig. 7(c)] and on the linear dependence on the magnetic field for the ferromagnetic samples with $x \geqslant 0.076$ [Fig. 7(c)]. The quadratic contribution to the MR for the paramagnetic samples with $x \leqslant 0.025$ and the linear contribution to the MR for the ferromagnetic samples with $x \geqslant 0.076$ is subtracted from the MR for these samples [typical results after subtraction are shown in the insets of Figs. 7(a) and 7(c)]. That leaves the pure SdH oscillatory component of the MR. The $\rho_{xy}(B)$ dependence for these samples confirms the presence of quantization of conduction energy levels by the appearance of the plateaus at magnetic fields higher than 3 T.

The frequency of the SdH oscillations can be used to calculate the carrier concentration in the material. This method of carrier-concentration calculation is better than the low-field Hall-effect method since it is unaffected by the assumption made in the Hall-effect analysis, i.e., the scattering factor equals 1. The number of the SdH oscillation for each of the studied temperatures plotted vs an inverse of the magnetic field shows a linear dependence [see representative curves in Fig. 7(b)]. The linear regression of the experimental SdH oscillation amplitude data [Fig. 7(b)] allows the estimation of the period of the SdH oscillations, P. The representative fitted lines and the obtained linear fit parameters are gathered for the selected $\mathrm{Cd}_{1\text{-}x\text{-}y}\mathrm{Mn}_x\mathrm{Zn}_y\mathrm{SnAs}_2$ samples in Fig. 7(b). The period of the SdH oscillations, P, obtained from linear regression of the experimental MR data allows the carrier concentration n_s to be calculated via the following equation:

$$n_s = \frac{1}{3\pi^2}\left(\frac{2e}{\hbar c P}\right)^{\frac{3}{2}}, \qquad (4)$$

where $\hbar$ is the Planck constant divided by 2π and the Fermi surface is assumed to be spherical. Using Eq. (4), we calculated the carrier concentration for all of our samples showing SdH oscillations at $T \leqslant 50$ K. The carrier concentration calculated from the SdH oscillation analysis does not change as a function of temperature. The n_s values obtained at $T \approx 1.5$ K are presented in Table II. As we can see, $n_s \approx n$ for all of our samples. It is a signature that the scattering factor for our samples is indeed close to 1 and the Hall-effect analysis was performed correctly.

The temperature dependence of the peak amplitude of the SdH oscillations, A, normalized to the amplitude at the lowest measured temperature, A_0, can be described with the use of the Lifshitz-Kosevich formalism [20]. The amplitude of the SdH oscillations follows the equation

$$\frac{A(T)}{A_0} = \frac{\xi}{\sinh\xi}, \quad \xi = \frac{2\pi^2 k_B T}{\hbar\omega_c}, \qquad (5)$$

where k_B is the Boltzmann constant, and $\omega_c = eB/m^*$ is the cyclotron frequency. We fit the experimental temperature dependencies of the SdH oscillation amplitudes obtained for all of our samples to Eq. (5) with the cyclotron frequency as the fitting parameter. Selected, representative data and the fit are presented in the inset of Fig. 7(f). From the obtained ω_c values, we calculated the effective mass m^* for most of our samples. The calculated m^* values are gathered in Table II. The obtained m^* values for all of our samples are similar and equal to about $0.11\text{–}0.12 \cdot m_e$, where m_e is the free electron mass. The effective mass of CdSnAs_2 is known in the literature to have values from $0.04m_e$ to $0.06m_e$ [21]. Higher m^* values obtained for our samples are most probably the result of alloying, which can influence the carrier transport in a material.

The theory of magnetoresistance oscillations was first developed by Adams and Holstein [22]. The oscillatory part of the electrical conductivity, taking into account the mechanisms leading to Landau-level broadening, can be described using the following equation [23]:

$$\begin{aligned}\ln\left[\frac{AB^{1/2}}{T}\sinh\left(\frac{\beta T m^*}{B}\right)\right] &= \ln\left|\frac{5}{2\sqrt{2}}\left[\frac{2e}{\hbar c(3\pi^2 n)^{\frac{2}{3}}}\right]^{\frac{1}{2}}\right.\\ &\quad\left.\times\,\beta m^*\cos\left(\frac{2\pi m^*}{|g^*|}\right)\right| - \frac{\beta T_D m^*}{B}, \qquad (6)\end{aligned}$$

where $\beta = 2\pi^2 k_B m_e/\hbar e$, g^* is the effective electron spin-splitting factor, and T_D is the Dingle temperature. The known m^* values can be used to determine T_D values by fitting the oscillatory part of the MR curves to Eq. (6). Equation (6) is linear in the $\ln\left[\frac{AB^{1/2}}{T}\sinh\left(\frac{\beta T m^*}{B}\right)\right]$ vs $1/B$ coordinates, namely conventional Dingle plot coordinates. It is therefore convenient to plot the experimental data in the form of a conventional Dingle plot, as presented in Fig. 7(d). It allows T_D estimation, since T_D is proportional to the slope of the experimental curves plotted on the Dingle plot. We made the data analysis based on plotting SdH data using the relation given by Eq. (6) for all our samples and for MR data obtained at $T < 50$ K. The representative Dingle plot obtained for the selected $\mathrm{Cd}_{1\text{-}x\text{-}y}\mathrm{Mn}_x\mathrm{Zn}_y\mathrm{SnAs}_2$ sample with $x = 0.025$ and $y = 0.028$ at $T = 1.6$ K is presented in Fig. 7(d). All of the obtained Dingle plots described by Eq. (6) show nearly linear behavior. The slope of the Dingle plot described by Eq. (6) obtained for all studied temperatures for each of our samples can be used to estimate the value of the Dingle temperature, T_D. The estimated T_D values for each of our samples are gathered in Table II. As we can see, the obtained T_D values are lower than 15 K, indicating rather large structural disorder of our samples. We can see a nonmonotonic increase of T_D with x, indicating an increasing disorder caused be the addition of Mn ions to the $\mathrm{Cd}_{1\text{-}x\text{-}y}\mathrm{Mn}_x\mathrm{Zn}_y\mathrm{SnAs}_2$ crystals.

The obtained T_D values can be used to calculate the scattering time, $\tau_D = \hbar/2\pi k_B T_D$, followed by the estimation of the carrier mobility, $\mu_D = e\tau_D/m^*$. The obtained values of μ_D are 8–9 times lower than the values estimated from the

Hall-effect data. The relation $\mu > \mu_D$ is expected [24] and is due to the fact that μ is sensitive to scattering events that change the direction of the electron while μ_D is sensitive both to the scattering effects and to the destruction of the phase coherence of electron wave functions, leading to broadening of the Landau level and reducing the amplitude of the SdH oscillations.

VI. SUMMARY

We explored the structural, magnetic, and electrical transport properties of $Cd_{1-x-y}Mn_xZn_ySnAs_2$ crystals with the average Mn contents x changing from 0.013 to 0.170 and Zn contents y varying from 0.002 to 0.051. Both structural and magnetic studies indicate that the Mn ions can be diluted in the host lattice up to about $x \approx 0.025$. For higher x values, the presence of hexagonal MnAs clusters is observed, resulting in a ferromagnetic order with the Curie temperatures around 305 K.

The magnetotransport studies showed that all investigated samples are n-type semiconductors with high carrier concentrations, n, equal to about 0.9–2.2 × 10^{18} cm^{-3}. All of our samples show high carrier mobilities μ changing in a nonmonotonic way with either x or y up to a maximum value of about 7100 $\mathrm{cm}^2/(\mathrm{V\,s})$ for the sample with $x = 0.025$ and $y = 0.028$. The Shubnikov–de Haas oscillations are present at $T \leqslant 50$ K for all our samples. The oscillations allowed the calculation of the effective mass m^*, giving values of about 0.11–$0.12 m_e$. The presence of magnetic impurities has a strong influence on the magnetoresistance of the alloy. For the samples with $x \geqslant 0.076$, the Shubnikov–de Haas oscillations are observed on the background of a large linear positive MR. Linear MR is present up to the room temperature, with maximum values of about 200% for the sample with $x = 0.170$ and $y = 0.002$ at $T = 1.5$ K. This positive MR is related to the presence of MnAs clusters in the semiconductor lattice.

[1] J. Kossut and W. Dobrowolski, *Handbook of Magnetic Materials* (North-Holland, Amsterdam, 1993), p. 231305.

[2] W. Dobrowolski, J. Kossut, and T. Story, *Handbook of Magnetic Materials* (Elsevier, Amsterdam, 2003), Chaps. II-VI, p. 289377.

[3] T. Dietl, Nat. Mater. **9**, 965 (2010).

[4] S. C. Erwin and I. Žutić, Nat. Mater. **3**, 410 (2004).

[5] S. Picozzi, Nat. Mater. **3**, 349 (2004).

[6] L. Kilanski, M. Górska, W. Dobrowolski, E. Dynowska, M. Wójcik, B. J. Kowalski, J. R. Anderson, C. R. Rotundu, D. K. Maude, S. A. Varnavskiy, I. V. Fedorchenko, and S. F. Marenkin, J. Appl. Phys. **108**, 073925 (2010).

[7] L. Kilanski, W. Dobrowolski, E. Dynowska, M. Wójcik, B. J. Kowalski, N. Nedelko, A. Ślawska-Waniewska, D. K. Maude, S. A. Varnavskiy, I. V. Fedorchenko, and S. F. Marenkin, Solid State Commun. **151**, 870 (2011).

[8] I. V. Fedorchenko, L. Kilanski, I. Zakharchuk, P. Geydt, E. Lahderanta, P. N. Vasilyev, N. P. Simonenko, A. N. Aronov, W. Dobrowolski, and S. F. Marenkin, J. Alloys Comp. **650**, 277 (2015).

[9] L. Kilanski, I. V. Fedorchenko, M. Górska, A. Ślawska-Waniewska, N. Nedelko, A. Podgórni, A. Avdonin, E. Lahderanta, W. Dobrowolski, A. N. Aronov, and S. F. Marenkin, J. Appl. Phys. **118**, 103906 (2015).

[10] W. X. Feng, D. Xiao, J. Ding, and Y. G. Yao, Phys. Rev. Lett. **106**, 016402 (2011).

[11] B. A. Bernevig, T. L. Hughes, and S.-C. Zhang, Science **314**, 1757 (2006).

[12] W. J. Paszkowicz, J. Appl. Crystallogr. **22**, 186 (1989).

[13] P. N. Hai, K. Takahashi, M. Yokoyama, S. Ohya, and M. Tanaka, J. Magn. Magn. Mater. **310**, 1932 (2007).

[14] P. J. Wellmann, J. M. Garcia, J. L. Feng, and P. M. Petroff, Appl. Phys. Lett. **71**, 2532 (1997).

[15] I. T. Yoon, T. W. Kang, and D. J. Kim, J. Magn. Magn. Mater. **320**, 662 (2008).

[16] L. Kilanski, K. Szałowski, R. Szymczak, M. Górska, E. Dynowska, P. Aleshkevych, A. Podgórni, A. Avdonin, W. Dobrowolski, I. V. Fedorchenko, and S. F. Marenkin, J. Appl. Phys. **114**, 093908 (2013).

[17] L. Kilanski, M. Górska, E. Dynowska, A. Podgórni, A. Avdonin, W. Dobrowolski, I. V. Fedorchenko, and S. F. Marenkin, J. Appl. Phys. **115**, 133917 (2014).

[18] E. L. Nagaev, Phys. Rep. **346**, 387 (2001).

[19] L. Kilanski, A. Reszka, M. Górska, V. Domukhovski, A. Podgórni, B. J. Kowalski, W. Dobrowolski, I. V. Fedorchenko, A. N. Aronov, and S. F. Marenkin, J. Phys.: Condens. Matter **28**, 495802 (2016).

[20] I. M. Lifshitz and A. M. Kosevich, Zh. Eksp. Teor. Fiz. **29**, 730 (1955).

[21] J. L. Shay and J. H. Wernick, *Ternary Chalcopyrite Semiconductors: Growth, Electronic Properties, and Applications* (Pergamon, Oxford, 1975).

[22] E. N. Adams and T. D. Holstein, J. Phys. Chem. Solids **10**, 254 (1959).

[23] D. G. Seiler and A. E. Stephens, *Landau Level Spectroscopy* (Elsevier, Amsterdam, 1991), Vol. 27.2, Part IV, p. 10311181.

[24] T. Dietl, J. Phys. Colloques **39**, C6-1081 (1978).